Experimental measurement of stress at a 4-domain junction in lead zirconate titanate

Ian MacLaren[a)]

Department of Physics and Astronomy, University of Glasgow, Glasgow G12 8QQ, UK

Ljubomira A. Schmitt and Hartmut Fuess

Institut für Materialwissenschaft, TU-Darmstadt, Petersenstr. 23, D-64287 Darmstadt, Germany

Hans Kungl and Michael J. Hoffmann

IKM, Universität Karlsruhe (TH), D-76131 Karlsruhe, Germany

A junction between two lamellar bands of ferroelectric domains in a lead zirconate titanate (PZT) ceramic is analysed using Kikuchi diffraction patterns in the transmission electron microscope. Indexing of the diffraction patterns allowed the determination of the 3D relative orientation of the 4 different domains at the junction and thus the characterisation of the domain boundaries. The local c/a ratio could also be determined from the misorientations at the domain boundaries. Analysis of the data showed that large stresses were concentrated at the junction, and that this is inevitable at such band junctions. Such stress concentrations could act as nuclei for

[a)] Electronic mail: ian.maclaren@physics.org, formerly at Institut für Materialwissenschaft, Technische Universität Darmstadt, Petersenstr. 23, D-64287 Darmstadt, Germany

cracking of the ceramic under additional loading in service, perhaps particularly as a consequence of extended electromechanical cycling. Moreover, the stresses would increase with increasing c/a making the issues all the more serious for Ti-rich compositions having larger c/a ratios.

PACS: 61.72.Lk, 61.72.Mm, 68.35.Gy, 68.37.Lp, 77.80.Dj, 77.84.Dy

I. Introduction

$Pb(Zr,Ti)O_3$ (PZT) ceramics are well-known and well-used ferro- and piezo-electric materials. Despite the fact that they have been used and studied for over 50 years, there are many issues that are insufficiently well understood. For example, only in the last 10-15 years has significant attention been devoted to the issue of switching mechanisms and fatigue due to electrical and mechanical cycling (e.g. Jiang *et al.*[1,2], Nuffer *et al.*[3,4]). Also much attention has been focussed on understanding the details of the crystallographic phase relations in the system, ever since the recent discovery of a monoclinic phase in the system[5].

Ferroelectric materials undergo a phase transition from a high symmetry paraelectric phase to a lower symmetry ferroelectric phase on cooling through the Curie temperature with an associated distortion of the unit cell. Partly to minimise strain and partly to reduce the bulk polarisation to zero, each grain in a polycrystalline ceramic will split into several domains, each with a different orientation of the polar axis and unit cell distortion. The walls between these domains tend to lie on well-defined crystallographic planes in order to minimise mismatch and strain at the

walls[6,7], especially where the piezoelectric distortion is high. This often results in lamellar domain structures where two domains alternate whilst always separated by the same plane, as is often the case in $BaTiO_3$ and tetragonal phase PZT[8]. Because the grains in a polycrystal are constrained by their neighbours, more complex 3D domain structures are adopted in order to minimise shape change of the individual grains. Structures that fulfill this criterion for tetragonal ferroelectrics have been considered in detail by Arlt *et al.* [9,10]. This results in the adoption of a so-called "herringbone" domain structure above a certain critical grain size, whereby different bands of lamellar structures alternate in a grain. These result, however, in stress concentrations both within grains at the lamellar junctions[9,10] and at grain boundaries[11].

Whilst it is straightforward to image domains and domain walls using a variety of techniques including conventional light microscopy, scanning electron microscopy (SEM) and transmission electron microscopy (TEM), it is more difficult to directly determine the crystallographic relationship between domains. This is more usually inferred from the known structure of the material (from X-ray diffraction) combined with stereographic analysis of the angles between the intersections of the domain walls with the sample surface. It is, however, possible to directly determine the relative orientation of domains using diffraction techniques such as Kikuchi diffraction patterns in TEM or electron backscattered diffraction in SEM. Such diffraction patterns reveal the full 3D orientation of a crystal. Thus if two patterns are recorded from adjacent crystals or domains without tilting the goniometer, then the full relative orientation matrix relating the two crystals can be determined. Progress has been made on the automation of this on some TEM/CCD camera systems[12-15]. In the present work a manual method to index Kikuchi patterns in order to thereby obtain

information about the misorientations and strains associated with domain structures in a tetragonal PZT composition.

II. Experimental methods

Sample preparation and characterisation

Samples with a nominal composition of $(Pb_{0.965}La_{0.01}Sr_{0.02})(Zr_{0.45}Ti_{0.55})O_3$ were prepared by a mixed-oxide method from PbO, ZrO_2, TiO_2, La_2O_3 and $SrCO_3$ powders. The powders were milled in isopropanol for 3 hours using ZrO_2 milling balls. The resulting slurry was then separated from the milling balls and dried in a rotary evaporator at 70-80°C, further dried at 100°C for 2-3 days, and then calcined at 850°C in an Al_2O_3 crucible for 2 hours. The resulting powder was then milled in a planetary ball mill for 6 hours with ZrO_2 balls to destroy hard agglomerates and pressed uniaxially into 12 mm pellets using a pressure of 17.7 MPa followed by cold isostatic pressing at 400 MPa. These pellets were then heated at 5 °C min^{-1} to 1225°C under an oxygen atmosphere and sintered for 2 hours. To minimise PbO loss through sublimation the sample was sintered in a powder bed of $PbZrO_3$ and ZrO_2.

Samples for TEM examination were prepared by a standard procedure of polishing, disc cutting, dimpling and ion-milling. Samples were coated with a thin carbon coat to prevent charging in the TEM. Transmission electron microscopy was performed with a Philips CM20 TEM operated at 200 kV. Conventional bright field imaging was combined with convergent beam electron diffraction (CBED) to characterise both the microstructure and the crystallography of the domains.

It may be noted in the CBED patterns shown in this paper (Figures 4 and 5) that no higher-order Laue-zone (HOLZ) lines could be observed in the patterns, and that in general, the Kikuchi lines were somewhat diffuse. This is not surprising in PZT ceramics as the high average atomic number of the material results in high Debye-Waller factors for all reflections at room temperature seriously reducing their sharpness and intensity; this effect is particularly serious for higher-order reflections and they are in most cases completely invisible. The only way to get sharp HOLZ reflections would be to work at much lower temperatures, for instance using liquid nitrogen cooling. This would, however, completely change the stress state of the ceramic since c/a ratios are strongly temperature-dependent. Thus, it is not feasible to use HOLZ lines for studying the stress states of PZT ceramics at room temperature. For this reason, the method described below using the lower-order Kikuchi lines is the only direct method of *local* (nanoscale) stress measurement for these materials at these temperatures.

Crystallographic measurements from diffraction patterns

All PZT compositions form a simple cubic perovskite phase with the space group $Pm\bar{3}m$ above their Curie temperature. The PZT composition used in this study leads to the formation of a simple tetragonal perovskite crystal structure with space group P4mm (Number 99 in the International Tables for Crystallography Volume A[16]) below the Curie temperature (~ 360°C in this case). The symmetry elements in this space group are 2- and 4-fold rotations about the **c**-axis together with mirror planes on (100), (010), (110) and $(1\bar{1}0)$. All symmetry elements of the parent cubic phase on planes or lines with a component perpendicular to the c-axis are lost due to the non-centrosymmetric nature of this polar structure. Please note that for

generalised indices it should be explicitly noted that the crystal system is tetragonal and thus <110> is inequivalent to <101>, [17] is inequivalent to {001} and so on. This normal convention of representing equivalent planes and directions[16,18] was preferred to the mixed bracket notation of Hug *et al.*[19]. Rietveld refinement of a powder X-ray diffractogram from a pulverised sample of the ceramic used in this work yielded lattice parameters of a = 4.0202(2) Å, c = 4.1371(2) Å corresponding to a c/a ratio of 1.029[20].

A very common feature of tetragonal ferroelectrics is the presence of so-called "90°"-domain boundaries. These separate domains where the c-axis is rotated by approximately 90°. Perfect lattice matching between adjacent domains is only found on one given {101} plane (this can be derived using the arguments of Fousek and Janovec[6], for example) and normally results in the formation of lamellar structures of alternating domains as described above. The lattice matching at the interface has the consequence, however, that the angle between the two **c**-axes deviates from 90° as shown in Figure 1. Good examples of high resolution TEM image of such a boundaries can be seen in Stemmer *et al.*[21]. The angle, 90°-δ, can be simply determined from simple trigonometry as $2\tan^{-1}(a/c)$. For our c/a ratio of 1.029, 90°-δ = 88.36° and thus δ = 1.64°. Despite the fact that the boundaries are not atomically sharp, having a finite width of the order of 1 nm with less distorted unit cells in the wall core, this relationship between the c/a ratio and the angle 90°-δ has been found experimentally to be well preserved[21].

To determine the crystallographic orientation from a Kikuchi pattern close to a major zone axis, **Z**, the following procedure was used (see Figure 2). Two perpendicular Kikuchi lines were indexed, and the directions normal to these (reciprocal lattice vectors) were thereby also indexed. This gives two vectors $\mathbf{g}_1$ and

$\mathbf{g}_2$. The angles of the projections of these vectors onto the diffraction pattern from the horizontal, α and β were measured. The distance of the pattern centre (usually indicated with the microscope pointer) from the zone axis, *n*, was measured together with the angle of this direction from the horizontal, θ. Correction was always made for any rotation of the negatives either in the negative holder in the TEM or in the film scanner. The camera length, L, could be calibrated from the widths of the Kikuchi lines. The distance *n* could be converted to an angle of tilt from the zone axis using $\gamma = \text{atan}(n/L)$. This provided the input data for the calculations.

A unit vector from the zone axis in the direction of a point above the pattern centre could be defined by vector addition of the two vectors defined from the **g** vectors:

$$\mathbf{n}' = \frac{\mathbf{g}'_1}{|\mathbf{g}'_1|}\cos(\theta - \alpha) + \frac{\mathbf{g}'_2}{|\mathbf{g}'_2|}\cos(\beta - \theta) \tag{1}$$

Where $\mathbf{g}'_1$ and $\mathbf{g}'_2$ are the real lattice vectors parallel to the reciprocal lattice vectors, $\mathbf{g}_1$ and $\mathbf{g}_2$. All vectors were transformed to a Cartesian system prior to these calculations for simplicity. **n'**, $\mathbf{g}'_1$ and $\mathbf{g}'_2$ are not quite in the plane of the negative due to the tilt of the pattern centre from the zone axis. The beam direction can then be determined by adding the zone axis direction, **Z**, and **n'** in the correct proportions:

$$\mathbf{B} = \frac{(1+\tan(\gamma))L\mathbf{Z} + (1+\tan(\gamma))n\mathbf{n}'}{|(1+\tan(\gamma))L\mathbf{Z} + (1+\tan(\gamma))n\mathbf{n}'|} = \frac{L\mathbf{Z} + n\mathbf{n}'}{|L\mathbf{Z} + n\mathbf{n}'|} \tag{2}$$

A vector in plane perpendicular to both **B** and **n'** can be calculated as $\mathbf{B}\times\mathbf{n}'$. The vector **n** defining the direction in plane from the zone axis to the pattern centre can now be derived as:

$$\mathbf{n} = (\mathbf{B}\times\mathbf{n}')\times\mathbf{B} \tag{3}$$

Vertical and horizontal directions, **V** and **H**, in the pattern can then be determined by simple trigonometry and vector addition as:

$$\mathbf{V} = \mathbf{n}\sin(\theta) + \mathbf{B}\times\mathbf{n}\cos(\theta) \tag{4}$$

$$\mathbf{H} = \mathbf{n}\cos(\theta) - \mathbf{B}\times\mathbf{n}\sin(\theta) \tag{5}$$

The result of this is a matrix constructed from the three orthogonal vectors describing the orientation of the crystal as shown below with the three vectors **B**, **V**, and **H** each as a column vector:

$$\mathbf{M} = \begin{pmatrix} b_1 & v_1 & h_1 \\ b_2 & v_2 & h_2 \\ b_3 & v_3 & h_3 \end{pmatrix} \tag{6}$$

The rotation matrix describing the relative orientation of two domains can then be easily determined:

$$\mathbf{M}_2 = \mathbf{R}\mathbf{M}_1 \Rightarrow \mathbf{R} = \mathbf{M}_2\mathbf{M}_1^{-1} \tag{7}$$

The axis/angle pair, (**r**,θ), describing the rotation was then extracted from the rotation matrix and the axis, **r**, converted back to tetragonal indices. For a specific boundary, a number of trial indexing schemes can be used and one will typically fit much better than the others. Thus the results (at least in the examples in this paper) were mostly unambiguous.

III. Results and Discussion

Structural characterisation of a domain boundary junction

Figure 3a shows a bright field image of a grain in the tetragonal PZT sample where the normal lamellar domain structure is clearly apparent. Closer inspection shows that it actually consists of two lamellar regions separated by a slight kink region in the centre. A close-up of this kink region is shown in Figure 3b. A number of things may be immediately observed. Every second domain appears to be continuous through the kink region, although some fringe contrast may be seen in the kink region itself. The other domains show a more abrupt change in image contrast at this junction, together with stronger fringe contrast. Also, some of these latter domains end at the junction and do not connect to domains on the other side. The fringe contrast probably arises as a kind of Δw fringe contrast due to the small crystallographic misorientation between the two domains at the boundary[22]. The near-uniformity of image contrast in domains away from the junction testifies that the sample is relatively flat and was not significantly bent in preparation, apart from perhaps at the very thinnest regions (not used in this analysis). The images were recorded with the sample oriented close to a <110> or <101> axis and are multibeam images. This allows the approximate projection of a number of crystallographic directions to be seen.

The sample was then tilted so that a CBED pattern from position *a* was perfectly aligned with the axis. CBED patterns were then recorded from positions *b*, *c* and *d* without changing the tilt angles on the goniometer and these are shown in Figure 4. It is clear that domain *b* is oriented so that the pattern centre sits somewhat to the right of the zone axis, that domain *c* is oriented so that the pattern centre is to the left of the zone axis, and finally that domain *d* is only slightly misoriented to the right from the zone axis.

In order to distinguish between the rather similar <110> and <101> axes it is necessary to tilt each domain on axis and examine the pattern symmetry in detail. As pointed out above many of the symmetry elements of the cubic perovskite $Pm\bar{3}m$ structure are lost on transformation to the tetragonal P4mm structure below the Curie temperature. In particular the mirror planes on (010) and on {101} planes are lost (i.e. (101), $(10\bar{1})$, (011) and $(01\bar{1})$). However the other mirror planes on (100), (010), (110) and $(1\bar{1}0)$ are retained. Similarly, the 2-fold rotation axis axes about all <101> directions are lost. The reader is referred to the International Tables for Crystallography Volume A[16] for further details.

If one considers the <110> and <101> axes, the following conclusions can be reached:

- Along the [110] axis the only symmetry element will be a mirror plane on $(1\bar{1}0)$, similar applies for other <110> axes.
- Along the [101] axis the only symmetry element will be a mirror plane on (010), similar applies for the other <101> axes.

Thus, it is relatively easy to use the symmetry in a CBED pattern to distinguish between these two otherwise similar looking axes of a tetragonal perovskite. Figure 5 shows zone-axis CBED patterns from each of the 4 positions marked in Figure 3b (the sample was tilted to the zone axis of each position in turn).

Figure 6 shows schematic indexed diffraction patterns for the [110] and [101] axes. It is apparent that Figures 5a and 5d display a mirror on a [23] plane. Thus it can be concluded that both axes are <110> axes. Figures 5b and 5c on the other hand show a mirror on a {010} plane. It is therefore clear that these two domains are oriented along <101> axes.

In order to start the indexing of the patterns, an arbitrary choice of the unit cell orientation for one of the domains must be made from the different symmetrically equivalent variants. Domain *a* was oriented along a <110> axis, and the unique choice was made to index this as $[1\bar{1}0]$. The four different indexing schemes were tried for domain *b* corresponding to rotations of 90°±δ about the four <100> axes. The best match was achieved when $[10\bar{1}]$ was indexed as the zone axis in domain *b*. This corresponds to a rotation of 88.94° about the axis [-1.00000, 0.00047, 0.00298], which is only 0.18° from the $[\bar{1}00]$ axis. From this 90°-δ value we can deduce a *local* c/a ratio of 1.019 which is close to, although a little lower than the bulk c/a ratio from X-ray diffraction of 1.029.

Similarly, if one starts from domain *d* which appears to be only slightly misoriented from domain *a*, and is also a <110> axis, then there are only two possible relative orientations to domain *a*. Either they are the same domain and one indexes it also as a $[1\bar{1}0]$ orientation, or it is a 180° domain. There is insufficient evidence from the image contrast to determine whether or not it is a 180° domain since the image contrast between areas *a* and *d* is dominated by strain contrast and possibly some fringe contrast from the boundary (a relatively large area of boundary is visible as it is almost perpendicular to the beam). If this domain *d* is indexed as being close to $[1\bar{1}0]$ then the best fit for the rotation from domain *c* to domain *d* is given by indexing domain *c* as $[0\bar{1}1]$. This corresponds to a rotation of 88.3° about the common axis [0.00183, -1.00000, 0.00045], which makes an angle of 0.11° with $[0\bar{1}0]$. This angle of 88.3° corresponds to a local c/a ratio of 1.030, very close to the X-ray value of 1.029.

Thus, it is clear from this that domains *a* and *d* have the same direction of the c-axis (although the sense is undetermined), *b* has one of the other possible orientations and *c* has the third possible orientation. Thus, we are dealing with an area where two lamellar structures meet between domain variant *a* and *b* and between domain variant *a* or $d \equiv \bar{a}$ and *c*. Such domain structures have been described previously by Arlt and co-workers[9,10] and were found to be very common in larger grained $BaTiO_3$. This was described as the α type domain structure and is schematically represented in Figure 7a. The slice through the three-dimensional structure of Figure 7a made by our TEM specimen is represented by the grey shaded region and is redrawn in Figure 7b for simplicity and clarity.

It is clear from this representation that if two domains are separated at the vertical junction of Figure 7a by a "90°" domain boundary (in our case domains *b* and *c*), then the other two are separated by a 180° domain boundary (in our case *a* and *d*). Thus, it becomes necessary to re-index the results given above for domains *c* and *d*. If we rotate domain *d* by 180° about the [010] axis then this gives a new indexing for the beam direction of close to $[\bar{1}\,\bar{1}\,0]$. The best fit of the rotation from domain *c* to domain *d* for something that corresponds to a 90°-δ domain boundary is then a beam direction close to $[0\,\bar{1}\,\bar{1}]$ for domain *c*. The rotation then corresponds to 88.3° about the common axis [-0.00183, -1.00000, -0.00045], which is as before 0.11° from $[0\,\bar{1}\,0]$.

Now that the *ad* boundary has been identified as a 180° boundary, the relative orientations of domains *a* and *d* and of domains *b* and *c* can be considered. It may perhaps be expected that there should be no rotation between domains *a* and *d*, except for the 180° rotation about some axis perpendicular to the [001] polarisation axis.

This, is however not the case and some strain contrast is visible at the interface and there is a clear change in the excitation of diffracted beams from one side to the other in Figure 3 with domain *d* significantly darker than domain *a*. This is born out by the CBED patterns of Figure 4 showing a slight tilt of domain *d* away from the <110> zone axis. This tilt can be quantified as 0.58° about the [0.016, 0.986, -0.160] axis, which makes an angle of 9.5° with [010].

Meanwhile if all were ideal then the rotation between domain *b* and domain *c* would correspond to a 90°-δ rotation about a <100> direction (plus an additional symmetry rotation of 90° about [001], see the next section for details). This is clearly not the case and the deviation from this is quite large: 1.78° about [-0.664, 0.088, -0.743].

Strain at band junctions between different lamellar regions

To understand these deviations from ideality, one has to consider the non-orthogonality of the domains. If all the rotations were 90° then there would be no mismatch. A rotation of [100]/90° from *b* to *a*, followed by a rotation of [010]/180° from *a* to *d*, followed by a rotation of [010]/90° from *d* to *c* would represent the sequence of rotations performed on going round the domain structure determined above if δ=0. The rotation from *b* to *c* could then be represented as

$$\mathbf{R}_{bc} = \mathbf{R}_{dc}\mathbf{R}_{ad}\mathbf{R}_{ba} = \begin{pmatrix} 0 & 0 & -1 \\ 0 & 1 & 0 \\ 1 & 0 & 0 \end{pmatrix}\begin{pmatrix} -1 & 0 & 0 \\ 0 & 1 & 0 \\ 0 & 0 & -1 \end{pmatrix}\begin{pmatrix} 1 & 0 & 0 \\ 0 & 0 & 1 \\ 0 & -1 & 0 \end{pmatrix} = \begin{pmatrix} 0 & -1 & 0 \\ 0 & 0 & 1 \\ -1 & 0 & 0 \end{pmatrix} \quad (8)$$

This corresponds to something more than a pure 90° rotation about [100] or [010] but closer inspection shows that the cell has simply been additionally rotated by

90° about [001]. This is a symmetry operation of the tetragonal system so we can rotate the cell by [001]/90° without changing the physical situation, this is performed below and the resulting matrix then describes a $[0\bar{1}0]$/90° rotation as expected:

$$\mathbf{R}_{[001]/90}\mathbf{R}_{bc} = \begin{pmatrix} 0 & 1 & 0 \\ -1 & 0 & 0 \\ 0 & 0 & 1 \end{pmatrix}\begin{pmatrix} 0 & -1 & 0 \\ 0 & 0 & 1 \\ -1 & 0 & 0 \end{pmatrix} = \begin{pmatrix} 0 & 0 & 1 \\ 0 & 1 & 0 \\ -1 & 0 & 0 \end{pmatrix} \quad (9)$$

As should be clear, performing these rotations with $\delta \neq 0°$ cannot return the original orientation. Thus, there will necessarily be some strain and bending somewhere in the domain structure. This can be illustrated by the following example. If we assume that the domains *a* and *d* are in fact perfectly aligned (apart from the 180 degree rotation) and that the rotations from *a* to *b* and from *d* to *c* are as expected for the 90°-δ value given for our measured c/a ratio of 1.03, then we can calculate the resulting mismatch between *b* and *c* as follows:

$$\mathbf{R}_{bc}^{real} = \mathbf{R}_{[001]/90}\mathbf{R}_{dc}\mathbf{R}_{ad}\mathbf{R}_{ba} \text{ and } \mathbf{R}_{mismatch} = \mathbf{R}_{bc}^{ideal^{-1}}\mathbf{R}_{bc}^{real} \quad (10)$$

Following the domain structure deduced above rotation $\mathbf{R}_{ba}$ corresponds to [100]/88.3°, $\mathbf{R}_{ad}$ to [010]/180°, and $\mathbf{R}_{dc}$ to [010]/88.3°. When one performs this sequence of rotations $\mathbf{R}_{\text{mismatch}}$ can be derived. This rotation corresponds [-0.583, -0.583, -0.566]/2.96º. It is therefore clear that such a junction between lamellar regions will have a large mismatch between the correct angle for meeting between one pair of domains (for instance those separated by the 180º domain boundary) and the other pair separated by the 90°-δº domain boundary. This will result in large stress concentrations at such boundaries.

One could characterise this angular mismatch at the junction of the four domains as a disclination[24]. In the present case, we formally have a disclination of one sign at the lower junction and one of the opposite sign at the upper junction. This

is illustrated on Figure 3b with the ⊗ and ⊙ symbols. Thus the structure described above of rotationally mismatched domains can fully equivalently be described as an array of disclination dipoles. The long-range strains of the individual disclinations would be cancelled by the strain fields of the neighbouring disclinations of opposite sign leaving only stress in the immediate vicinity of the disclinations. This would allow the presence of disclinations, whereas they are not normally found in crystals due to the extremely high energy associated with the unrelaxed long-range strain field except for the case of liquid crystals where shear moduli are relatively low[25]. Such a model has previously been discussed for such band junctions in Ferroelectrics[26]; the present study shows the first direct experimental verification of this model.

Following Arlt[9] one would expect that the two boundaries *ab* and *cd* should be more or less normal 90°-δ boundaries with little deviation from the ideal rotation angle since these boundaries will have a much larger surface area than the boundaries *ad* and *bc*. This is confirmed by our analysis of the electron diffraction patterns, and this shows that the twinning angle is preserved despite any finite thickness that the boundaries may have, in accordance with the previous results of Stemmer *et al.*[21]. This also confirms that despite the relatively small thickness of the TEM sample, the crystallography of the standard lamellar domain structures is well preserved. Since the boundaries *ad* and *bc* are mostly unstrained, the majority of the strain will be concentrated at the *ad* and *bc* boundaries, as also observed in the TEM images and diffraction patterns shown above. Of course in the thin TEM specimen some of the three dimensional constraint has been lost which would have been present in the bulk material, and the *bc* boundary seems to be much more stressed than the *ad* boundary, although strain contrast is present at both.

This mismatch strain was first considered by Arlt and co-workers[9,10] who estimated the extra energy caused by constraining the 90°-δ domain walls across the junction to fit (such as the *b* to *c* boundary), this was further refined by Pertsev and Arlt[26]. Their considerations do not perhaps calculate the mismatch angles or axes as rigorously as was performed above with matrices but clearly show that a large amount of strain energy is stored in such junctions between different lamellar regions. Thus, such banding of grains into different lamellar regions only occurs above a certain critical grain size where the extra energy from such junctions is less than that of the stress to the grain as a whole for not adjusting shape in 3 dimensions. As Arlt *et al.*[10] point out, this critical grain size will be smaller for PZT than for the $BaTiO_3$ mainly studied by them due to the higher c/a ratio of tetragonal PZT.

It should be noted that the mismatch angle, α, resulting from the 3 combined rotations is rather higher than the δ angle for c/a. It would be complex to write an analytical equation for this angle but it is easily calculated numerically from the matrix multiplication of (6) and is plotted against c/a in Figure 8. The α/δ ratio is not quite constant but only increases slowly with c/a from about 1.73 to 1.75 in the range of the graph. In Arlt[9,10] the angle that was used, $\beta \approx \delta$, as defined in this paper.

Now the mismatch strain concentrated across the boundaries *ad* and *bc* could be accommodated elastically in the crystal, or could be at least partly accommodated by arrays of edge dislocations contained in these boundaries. Such dislocations have not yet been observed, but it is still possible that they exist, perhaps with a smaller spacing than could be observed in bright field TEM. Nevertheless, simple calculations can be used to at least set upper limits on the strains that could be concentrated in the vicinity of such boundaries. If we assume rather conservatively that half of the bending is accommodated across the *ad* boundary and half across the

bc boundary, then the relevant bend angle is $\alpha/2$. The bending seems to occur across 100 nm from examination of the contrast in Figure 3b. This gives a radius of curvature of:

$$r = 200/\alpha \tag{11}$$

The domains have a thickness, t, of about 100 nm. The peak tensile stress if the domains are approximated as parallel-sided bars is then:

$$\varepsilon_{max} = t/2r = t\alpha/400 \tag{12}$$

The Young's modulus for PZT is about 80 GPa[17] so we can translate this strain into a peak stress of 1.09 GPa for a c/a ratio of 1.03 as shown above. Of course, proper consideration of the geometry of the situation would adjust this figure somewhat. It is also the case that this strain could be reduced by the formation of edge dislocation networks in the boundaries. Thus, the peak stress will probably be a little lower than this, although of a similar order of magnitude and this illustrates very well the massive concentration of stress that occurs at these junctions between lamellae. It may of course be remarked that such high stresses are in excess of the yield strength of the ceramic. It is no doubt true that if such a large tensile stress were applied to a bulk PZT ceramic it would fracture instantaneously. Nevertheless, the bulk fracture strengths of ceramics are dominated by the effects of large surface defects such as open pores and scratches, and bear little relation to the intrinsic strength of the material. If the high strains discussed here are confined to 100 nm regions within grains, then such high stresses may not immediately crack the material due to the clamping effect of the surroundings.

This maximum (elastically accommodated) stress, σ_{Max}, is plotted against c/a on Figure 8. With increasing Ti content the c/a ratio increases to ultimately reach > 1.06 for $PbTiO_3$ with quite drastic consequences. In order to ensure the 3D

accommodation of strain, such domain banding with boundaries between different lamellar structures becomes increasingly necessary and the width of the bands will become smaller[10]. At the same time the stress concentrations at these junctions between the bands will increase higher and higher with the maximum stress predicted to reach over 2.5 GPa according to the calculations shown in Figure 8. Such a high stress level is almost certain to spontaneous microcracking as has frequently been observed for $PbTiO_3$ ceramics. Certainly when an additional strain is applied, for example in the form of an applied electrical field, this will further concentrate stress at these band junctions leading ultimately to crack nucleation and growth, resulting ultimately in material failure. This perhaps explains many of the difficulties in producing and using $PbTiO_3$ in ceramic form. It should also be noted that, where $PbTiO_3$ has successfully been sintered to a dense ceramic, this was only possible where the grain size was well controlled and kept as small as possible[27-31]. This would minimize the formation of such banded structures and their associated stress concentrations and should result in most domains having just one lamellar structure, although whether this was truly the case is not clear since the published studies on sintering of $PbTiO_3$ ceramics do not usually provide detailed micrographs of the domain structures.

It is also clear, that even for much lower c/a ratios typical of tetragonal PZT compositions, such as that examined in this article, junctions between different lamellar bands constitute significant stress concentrations. Particularly under the influence of applied fields, this could lead to further stress concentration and the nucleation of microcracks at the most highly stressed areas, resulting in mechanical damage to the material on repeated electrical cycling. Moreover, in order to achieve switching of a grain towards a single domain state under the influence of an electrical

field will require the movement of such junctions and thus the cooperative movement of all domain boundaries. This could alternatively be viewed as requiring the movement of the disclinations at the four-domain junctions through the material as the boundaries move. This would exert enormous local stresses and could also result in mechanical fatigue to the material. These processes could well explain the nucleation of microcracks in the bulk of a ferroelectric device (and not just close to the electrodes) as was observed by Nuffer *et al.*[3] for a commercial tetragonal PZT composition. Furthermore, the difficulty of moving the band junctions will contribute to the difficulty of achieving complete domain rotation in large grained PZT and may well be a significant contributory factor to the well-known "hard" piezoelectric properties of many tetragonal PZTs.

The magnitude of the stresses associated with such 4-domain junctions will be reduced at lower c/a ratios. Thus, compositions closer to the morphotropic phase boundary will experience fewer problems with this effect than those having higher Ti contents. In view of the totally different crystallography in the rhombohedral phase, the effect as described here will no longer be applicable in compositions to the Zr-rich side of the morphotropic phase boundary, although it is possible that analogous effects may occur in such compositions, albeit with different crystallographic details.

IV. Conclusions

A junction between two lamellar bands in a grain of a $(Pb_{0.965}La_{0.01}Sr_{0.02})(Zr_{0.45}Ti_{0.55})O_3$ ceramic has been studied using both bright field imaging and convergent beam diffraction in a transmission electron microscope. The crystallographic orientation of each domain was unambiguously determined from

CBED patterns and the four domain boundaries present at the junction were thus characterised. The domain boundaries in the lamellar regions to either side correspond to 90°-δ boundaries as expected but those at the junction contain additional strain. It was shown that this must necessarily be the case, as a consequence of the non-orthogonality of so-called "90°" domains. The angular mismatch at this band junction was demonstrated to be equivalent to an array of disclination dipoles at the four domain junctions as previously proposed by Pertsev and Arlt[26]. The resulting stress was calculated and peak stresses could exceed 1 GPa if not at least partially accommodated by additional defects, such as dislocation arrays in the boundaries. This would increase even further with increasing c/a ratio and it was shown that this might well explain the microcracking of coarse-grained $PbTiO_3$ ceramics either directly after sintering or on exposure to electric fields. It was also shown that such stress concentrations could result in premature mechanical failure of tetragonal PZT compositions and may contribute to the ferroelectric hardness of these compositions.

Acknowledgements

The authors would like to thank the Deutsche Forschungsgemeinschaft for financial support of part of this work through the Sonderforschungsbereich 595 "Elektrische Ermüdung von Funktionswerkstoffen" (special research area on the Electrical Fatigue of Functional Materials). Helpful discussions with Profs. J. Rödel, R.C. Pond, A. Craven and Drs. S.L. Dudarev, D.C. Lupascu and J.-J. Fundenberger are also gratefully acknowledged.

References

1. Q.Y. Jiang, E.C. Subbarao, and L.E. Cross, J. Appl. Phys., **75**, 7433 (1994).
2. Q.Y. Jiang, W.W. Cao, and L.E. Cross, J. Am. Ceram. Soc., **77**, 211 (1994).
3. J. Nuffer, D.C. Lupascu, A. Glazounov, H.J. Kleebe, and J. Rödel, J. Eur. Ceram. Soc., **22**, 2133 (2002).
4. J. Nuffer, D.C. Lupascu, and J. Rödel, J. Eur. Ceram. Soc., **21**, 1421 (2001).
5. B. Noheda, D.E. Cox, G. Shirane, J.A. Gonzalo, L.E. Cross, and S.E. Park, Appl. Phys. Lett., **74**, 2059 (1999).
6. J. Fousek and C. Janovec, J. Appl. Phys., **40**, 135 (1969).
7. P. Sapriel, Phys. Rev. B., **12**, 5128 (1975).
8. E.K.W. Goo, R.K. Mishra, and G. Thomas, J. Appl. Phys., **52**, 2940 (1981).
9. G. Arlt and P. Sasko, J. Appl. Phys., **51**, 4956 (1980).
10. G. Arlt, J. Mater. Sci., **25**, 2655 (1990).
11. Q.Y. Jiang, E.C. Subbarao, and L.E. Cross, Acta Met. Mater., **42**, 3687 (1994).
12. S. Zaefferer and R.A. Schwarzer, Z. Metallkunde, **85**, 585 (1994).
13. S. Zaefferer, J. Appl. Cryst., **33**, 10 (2000).
14. A. Morawiec, J. Appl. Cryst., **32**, 788 (1999).
15. J.J. Fundenberger, A. Morawiec, E. Bouzy, and J.S. Lecomte, Ultramicroscopy, **96**, 127 (2003).
16. International Tables for Crystallography, Volume A: Space-Group Symmetry, ed. T. Hahn (Kluwer Academic Publishers, Dordrecht, Netherlands, 2002).
17. A. Jimenez and J.M. Vicente, J. Phys. D, **33**, 1525 (2000).
18. P. Shang, T.T. Cheng, and M. Aindow, Philos. Mag. A, **79**, 2553 (1999).
19. G. Hug, A. Loiseau, and P. Véyssiere, Philos. Mag. A, **57**, 499 (1988).

20. L.A. Erac, Strukturelle Untersuchungen an Bleizirkoniumtitanaten, Diploma Thesis, (Technische Universität Darmstadt, Darmstadt, Germany, 2003).
21. S. Stemmer, S.K. Streiffer, F. Ernst, and M. Rühle, Philos. Mag. A, **71**, 713 (1995).
22. R.C. Pond, J. Microsc. (Oxford), **135**, 213 (1984).
23. X. Zhang, H. Wang, R.O. Scattergood, J. Narayan, C.C. Koch, A.V. Sergueeva, and A.K. Mukherjee, Appl. Phys. Lett., **81**, 823 (2002).
24. W.F. Harris, Philosophical Magazine, **22**, 949 (1970).
25. M. Kléman, The General Theory of Disclinations, in Dislocations in Solids, ed. F. R. N. Nabarro (North-Holland, 1980) Chapter 22, Vol. 5, pp. 243-297.
26. N.A. Pertsev and G. Arlt, Ferroelectrics, **132**, 27 (1992).
27. A. Udomporn, K. Pengpat, and S. Ananta, J. Eur. Ceram. Soc., **24**, 185 (2004).
28. H. Idrissi, A. Aboujalil, J.P. Deloume, G. Fantozzi, and B. Durand, J. Eur. Ceram. Soc., **19**, 1997 (1999).
29. S. Kim, M.C. Jun, and S.C. Hwang, J. Am. Ceram. Soc., **82**, 289 (1999).
30. C.G.S. Pillai and P.V. Ravindran, Thermochimica Acta, **278**, 109 (1996).
31. C.H. Lu and Y.P. Wu, Mater. Lett., **27**, 13 (1996).

Figure captions

Figure 1: A schematic diagram of a “90°”-domain boundary in a tetragonal perovskite formed by rotation about the [010] axis.

Figure 2: Schematic of the main measurements made on a negative of a Kikuchi pattern.

Figure 3: TEM images of the kinked lamellar structure in a $(Pb_{0.965}La_{0.01}Sr_{0.02})(Zr_{0.45}Ti_{0.55})O_3$ sample. a) Overview of the grain, the kink region is arrowed; b) close-up of a few domains at the kink, with the points used for CBED experiments marked.

Figure 4: CBED patterns from the 4 different areas marked in Figure 3b.

Figure 5: On-axis CBED patterns of the central discs from positions *a*, *b*, *c* and *d*. In some cases the pattern centre is very slightly offset from the exact zone axis. Nevertheless it is possible to recognise unambiguously the mirror plane in each pattern. The original greyscale images have been coloured using a colour scale to represent different grey levels, this has the advantage of making the extremes of contrast more easily visible, as well as improving the visibility of small contrast changes.

Figure 6: Schematic indexed diffraction patterns for the [110] and [101] axes of a tetragonal perovskite.

Figure 7: a) Schematic representation of the spatial domain configuration of the α type (after Arlt *et al.*[9]) with the approximate plane of the TEM specimen used in this work shown in light grey and the approximate beam direction shown as B. b) Schematic representation of the domain structure in the TEM specimen with all domain walls shown as striped regions.

Figure 8: Graph of δ, α and σ_{Max} against c/a, the two angles are plotted against the left hand axis and the stress against the right hand axis. Measured c/a values from Joseph *et al.*[31] for $PbTiO_3$ and PZT and from Kwei *et al.*[32] for $BaTiO_3$.

Figure 1

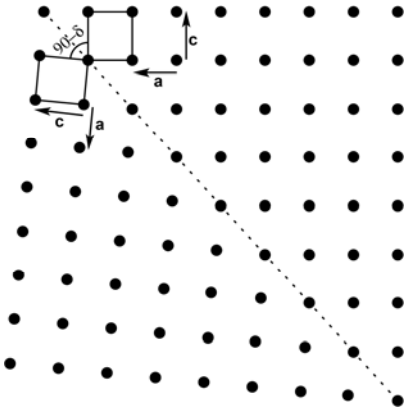

Figure 2

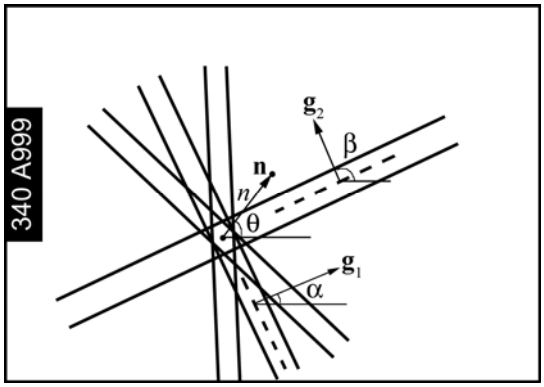

Figure 3

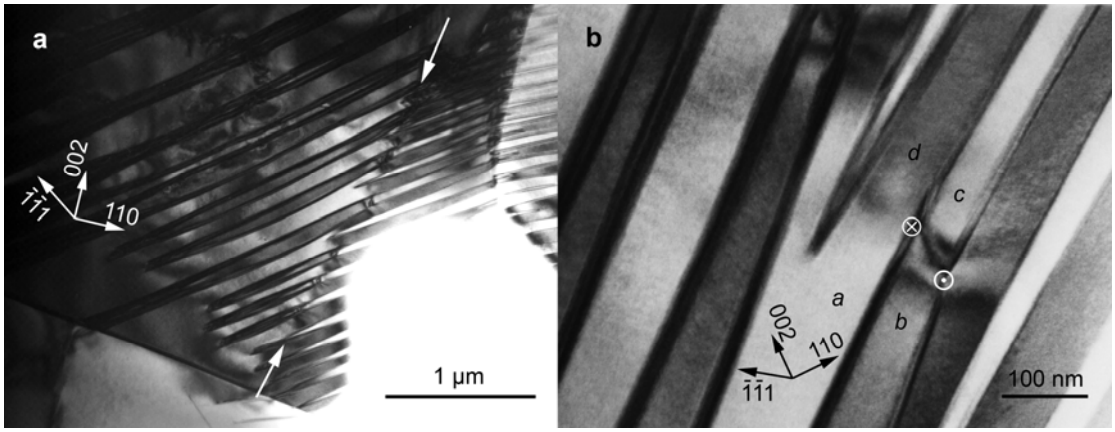

Figure 4

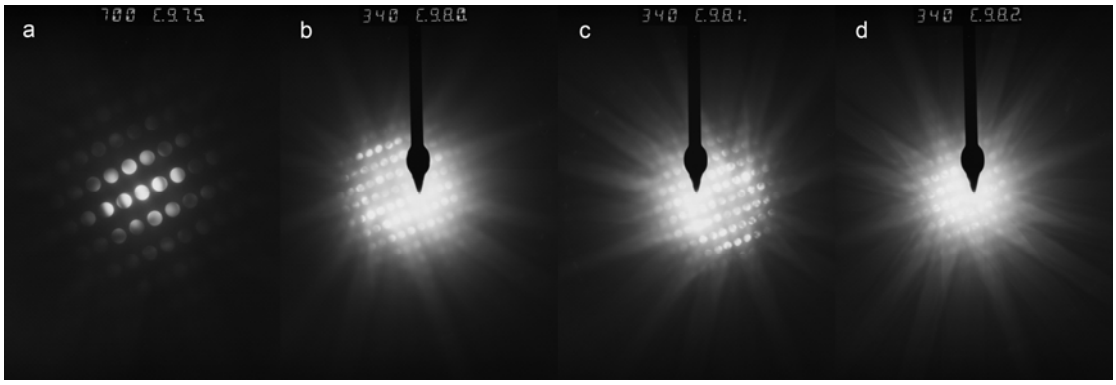

Figure 5

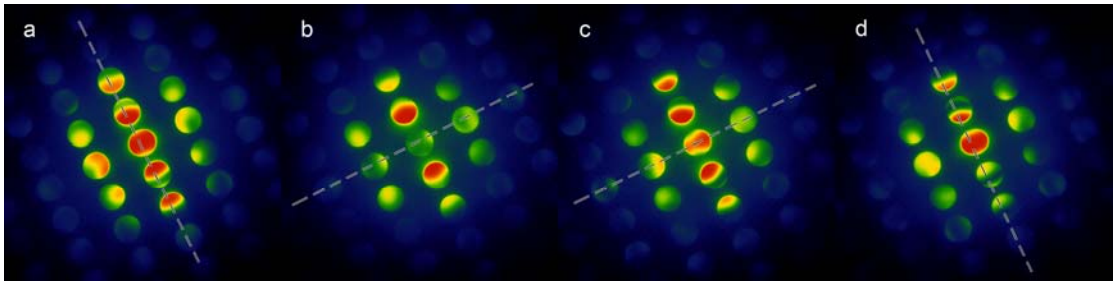

Figure 6

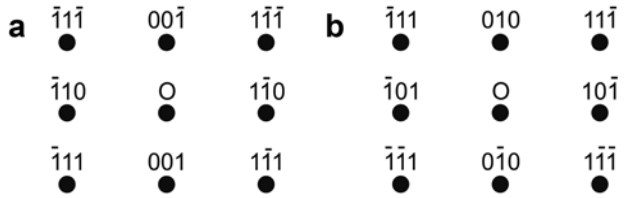

Figure 7

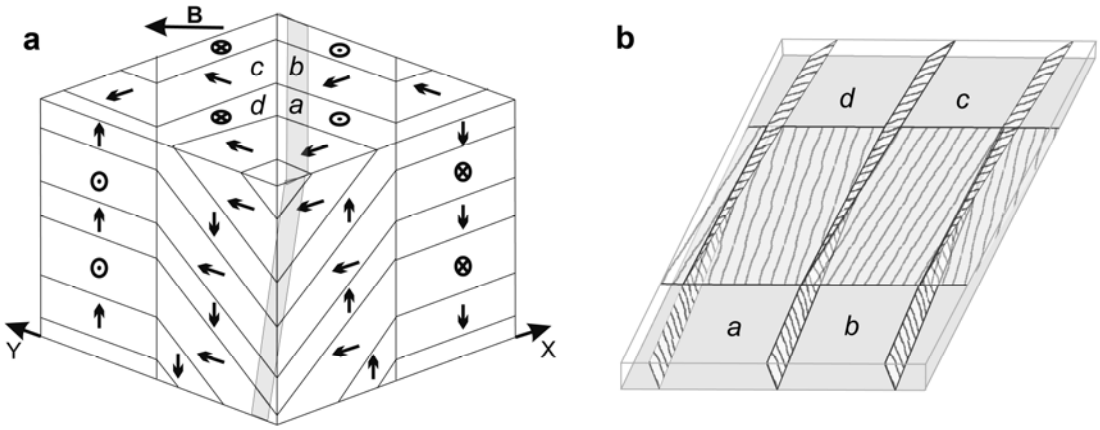

Figure 8